Machine-learning-based three-qubit gate design for the Toffoli gate and parity check in transmon systems

S. Daraeizadeh,[1,2] S. P. Premaratne,[2] N. Khammassi,[2] X. Song,[1] M. Perkowski,[1] and A. Y. Matsuura[2]
[1]*Department of Electrical and Computer Engineering, Portland State University, Portland, Oregon 97201, USA*
[2]*Intel Labs, Intel Corporation, Hillsboro, Oregon 97124, USA*

(Received 2 August 2019; accepted 26 March 2020; published 2 July 2020)

We use machine-learning techniques to design three-qubit entangling gates with fidelities of >99.9% and duration of 50 ns for nearest-neighbor coupled flux-tunable transmons in circuit quantum electrodynamics architectures. The gate design procedure enforces realistic constraints and analyzes the robustness of the new gates under decoherence, distortion, and random noise. The controlled-controlled-phase gate in combination with two single-qubit gates realizes a Toffoli gate which is widely used in quantum circuits, logic synthesis, and quantum error correction. We also introduce a three-qubit entangling Parity Checker gate which has applications in quantum arithmetic circuits and quantum error correction schemes. Using these three-qubit gates, we design a circuit for Shor's nine-qubit quantum error correction code and compare its performance to conventional realizations.

DOI: 10.1103/PhysRevA.102.012601

I. INTRODUCTION

Circuit quantum electrodynamics (cQED) [1,2] systems utilizing transmons [3–5] are potential candidates for realizing gate model quantum computers [6], with qubit coherence times of hundreds of microseconds [7] and the potential to scale up facilitated by quantum error correction schemes [8,9]. In these systems, the realization of high-fidelity single-qubit and two-qubit entangling controlled-phase (CZ) gates enables universal quantum computation [7]. However, it is desirable to design three-qubit entangling gates to achieve better performance in certain quantum circuits.

Multiqubit controlled-phase gates in transmons are typically designed by detuning the qubit transition frequencies to approach the avoided-level crossing regions. In this regime, state mixing or level shifting due to noncomputational quantum levels allows nonuniform phase collection within the computational subspace. This gives rise to entangling operations between qubits [10–15]. Finding the optimal transmon frequency detuning to achieve the desired avoided-level crossings between system energy levels is a complex task which can take advantage of machine-learning (ML) approaches [16–18]. Designing quantum gates and optimized control pulses using ML techniques and optimization theory has been demonstrated for various quantum systems [19–22]. We model the quantum gate design problem as a supervised ML exercise, by adjusting the system control parameters to converge to the target gate [17]. In this model, the training set is the desired unitary matrix and the cost function is the gate fidelity. We realize two types of three-qubit gates, the controlled-controlled-phase (CCZ) and the Parity Checker (ParChe) gates for transmon systems based on resonator-mediated nearest-neighbor (NN) couplings [23]. The CCZ gate collects a π rotation when all three qubits are in the state $|1\rangle$, while the ParChe gate collects a π rotation when the middle qubit is in the state $|1\rangle$ and the two distant qubits are in opposite states. Both gates are designed with duration 50 ns and gate fidelities of 99.99% and 99.975% for CCZ and ParChe gates, respectively. Moreover, the gates fidelities >99.9% are observed using simulated process tomography.

In Secs. II and III, we explain the motivation behind our work, introduce the CCZ and ParChe gates from a logic perspective, and discuss some of their applications in various quantum circuits. In Secs. IV and V, our simulation method and gate design methodology are explained, respectively. The gates are characterized in Secs. VI and VII. Finally, in Sec. VIII, we show how quantum error correction circuits can benefit from these gates by applying them to the circuit for Shor's nine-qubit error correction code [24].

II. MOTIVATION

Three-qubit gates have broad applications in quantum error correction [24,15], reversible computing [25,26], and quantum arithmetic circuits [27,28]. The Toffoli gate in combination with Hadamard gate are computationally universal [29,30]. However, typically multiqubit gates are decomposed into one-qubit and two-qubit gates depending on the available universal gate set in the physical quantum system [31]. The most common decomposition of the Toffoli gate using standard single- and two-qubit gates requires multiple single-qubit gates (H, T, and $T^\dagger$) and six two-qubit controlled-NOT (CNOT) gates [32]. In this decomposition, at least two of the CNOT gates are applied to non-neighboring qubits which results in the addition of four SWAP gates in a NN-coupled architecture; the total circuit depth is 16 steps. Another decomposition of the Toffoli gate with circuit depth of three is possible based on a three-qubit CCZ gate and two single-qubit gates [31]. The latter decomposition significantly reduces the cost of quantum circuits by improving the performance and lowering logical error rate. In this paper, our main goal is to improve the performance and the cost of quantum circuits by

designing high-fidelity single-shot three-qubit gates such as CCZ-based Toffoli gate for a resonator-mediated NN-coupled transmon system [23]. In Sec. III, we explain the realization of Toffoli (based on CCZ) and ParChe gates as well as how the quantum circuits can benefit from these three-qubit gates.

The experimental design of single-shot three-qubit gates is challenging due to the large state space and nonconvex control landscape [14,15]. The first experimental realization of a π rotation CCZ gate for three transmons coupled to a single resonator was designed by Reed *et al.* [15] via two engineered interactions within the state space. The higher complexity of the multiqubit gate design problem for transmons in cQED architecture requires leveraging ML techniques for improving fidelity and gate speed. Our goal is to use the machine-learning methods to realize multiqubit gates with the best fidelities possible in predefined reasonable gate times.

Although there are many machine-learning and optimal quantum control algorithms [16–22], the Subspace-Selective Self-Adaptive Differential Evolution (SUSSADE) [16] technique is particularly well suited for this study as it has been previously examined for designing high-fidelity multiqubit gates for a comparable system consisting of transmons with capacitive couplings. And, it is shown that SUSSADE outperforms greedy and global optimization algorithms such as quasi-Newton, and Differential Evolution, respectively [17]. Moreover, it is structured based on evolutionary algorithms which naturally enable the usage of parallel programming on high-performance computing systems [33].

Utilizing SUSSADE, we present an extensible gate design framework to design robust and high-fidelity single-shot multiqubit gates. Key features of this work include the following:

(1) The framework uses SUSSADE only to reduce the search space. It then employs a repetitive sequential local search algorithm to fine-tune the control parameters. The combined search algorithms enable faster realization of high-fidelity quantum gates for complex systems.

(2) Realistic experimental constraints are enforced during the initialization and learning phases.

(3) The gates are characterized comprehensively using simulated quantum process tomography and noise modeling.

III. REALIZATION OF TOFFOLI AND ParChe GATES

The typical avoided-level crossing used for two-qubit gates in transmons is between eigenstates $|11\rangle$ and $|02\rangle$ in a two-transmon system and these levels occupy the double-excitation manifold [10]. Here, we generalize this idea to a three-transmon system and consider the primary interactions up to the triple-excitation manifold. We steer the energy levels of the three-transmon system by detuning qubit transition frequencies such that the desired computational states each pick up a phase factor π, while all other energy levels collect trivial phases.

In our simulations, we consider the lowest four energy levels (labeled $|0\rangle$ to $|3\rangle$) to ensure system evolution within the full triple-excitation manifold [15]. However, the cost function evaluation for the ML approach is performed only within the computational subspace where each transmon may be in state $|0\rangle$ or $|1\rangle$. Consider an array of three NN-coupled qubits (L, M, and R). The CCZ gate is designed to collect a π phase only on the $|111\rangle$ computational state (i.e., when L, M, and R qubits are in the $|1\rangle$ state). The ParChe gate applies a π rotation only if qubit M is in state $|1\rangle$, and the first and the third qubits are in different states. In other words, if the exclusive-OR of the states of qubits L and R is 1, and qubit M is in state 1, then a π phase is collected. The matrix representations of the ideal CCZ and ParChe gates are as follows:

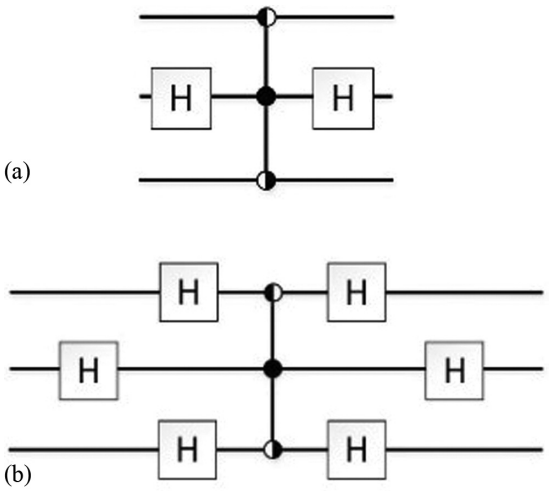

FIG. 1. Error syndrome detection circuits using the parity checker (ParChe) gate. (a) The bit-flip error syndrome detection circuit, (b) the phase-flip error syndrome detection circuit.

$$U_{\mathrm{CCZ}} = \begin{bmatrix} 1 & 0 & 0 & 0 & 0 & 0 & 0 & 0 \\ 0 & 1 & 0 & 0 & 0 & 0 & 0 & 0 \\ 0 & 0 & 1 & 0 & 0 & 0 & 0 & 0 \\ 0 & 0 & 0 & 1 & 0 & 0 & 0 & 0 \\ 0 & 0 & 0 & 0 & 1 & 0 & 0 & 0 \\ 0 & 0 & 0 & 0 & 0 & 1 & 0 & 0 \\ 0 & 0 & 0 & 0 & 0 & 0 & 1 & 0 \\ 0 & 0 & 0 & 0 & 0 & 0 & 0 & -1 \end{bmatrix}, \quad (1)$$

$$U_{\mathrm{ParChe}} = \begin{bmatrix} 1 & 0 & 0 & 0 & 0 & 0 & 0 & 0 \\ 0 & 1 & 0 & 0 & 0 & 0 & 0 & 0 \\ 0 & 0 & 1 & 0 & 0 & 0 & 0 & 0 \\ 0 & 0 & 0 & -1 & 0 & 0 & 0 & 0 \\ 0 & 0 & 0 & 0 & 1 & 0 & 0 & 0 \\ 0 & 0 & 0 & 0 & 0 & 1 & 0 & 0 \\ 0 & 0 & 0 & 0 & 0 & 0 & -1 & 0 \\ 0 & 0 & 0 & 0 & 0 & 0 & 0 & 1 \end{bmatrix}, \quad (2)$$

where the ordering of the states is $|000\rangle$ to $|111\rangle$ in binary increments. Following Fedorov *et al.* [14], and Reed *et al.* [15], we use the symbol of three filled dots for the three-qubit CCZ gates. Here, we introduce a symbol (see Fig. 1) for the ParChe gate where the first and the last dots are half filled with opposite orientation, indicating the first and the last control qubits are in opposite states, while the full dot on the middle qubit means that it must be in the state $|1\rangle$ for phase collection.

From a logic perspective, the proposed three-qubit ParChe gate is equivalent to two consecutive two-qubit CZ gates. Note that in our considered physical model [4], one cannot simply perform two CZ gates simultaneously on three transmons, since the effect of energy levels in three-excitation manifold needs to be considered. Utilizing the machine-learning techniques and optimization methods enable us to explore the state

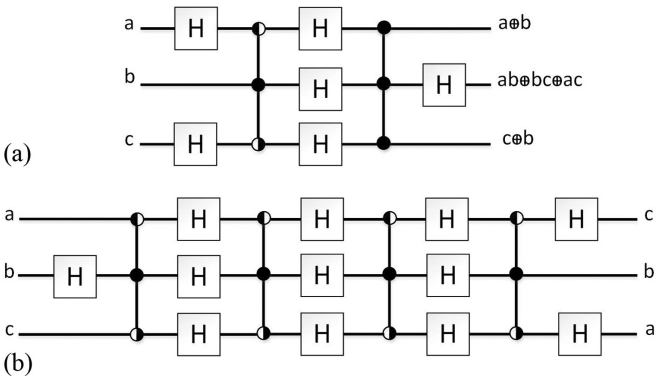

FIG. 2. Quantum circuits utilizing ParChe gate. (a) Majority function of three inputs is realized on the middle qubit. (b) The states of the first and the last qubits are swapped while the state of the middle qubit is unchanged.

mixing of all three transmons simultaneously and realize true single-shot three-qubit entangling gates such as ParChe gate.

The ParChe gate can be used in various quantum error correction (QEC) schemes [9] where a parity check is used to detect error syndromes. For example, in QEC stabilizer codes, including SURFACE CODE [34–36], the bit-flip and phase-flip error syndrome detection circuits can be implemented using ParChe gate as depicted in Figs. 1(a) and 1(b), respectively.

Utilizing ParChe and CCZ gates, one can efficiently realize a family of majority-based reversible gates [37]. For example, the ParChe gate in combination with one CCZ gate and single-qubit gates as depicted in Fig. 2(a) can realize a majority function of three inputs which is the "carry-out" in the Full adder circuits [38].

In technologies where the SWAP operations are decomposed to CNOT or CZ gates, one can use the ParChe gate to perform mirror-inversion (MI) operations [39,40] as shown in Fig. 2(b). Here, we consider a physical model that the single-qubit gates take 20 ns and two-qubit CZ gates take 40 ns [10,23,41]. In this physical model, the reported 40-ns duration for CZ gate covers the timing required to remove the extra phase collected on each qubit during the CZ operation. Therefore, for a fair comparison we add 10 ns to our three-qubit gate duration to accommodate for the phase compensation. The three-qubit MI operation based on 40-ns CZ gates would take 420 ns, while utilizing the 60-ns ParChe gates instead of CZ gates would result in a 19% performance improvement. Considering limited coherence time of near-term quantum systems, this performance improvement is of high importance.

The Fredkin gate is a three-qubit entangling gate which performs a controlled-SWAP operation, and it is an important universal gate with applications in reversible logic, quantum computing [42], and distributed secure quantum machine learning [43]. As depicted in Fig. 3, the Fredkin gate can be constructed using a CCZ gate and two CZ gates, in combination with single-qubit gates.

IV. SIMULATION OF THE SYSTEM DYNAMICS

The behavior of a superconducting qubit connected to a resonator is similar to the behavior of an atom in a cavity [1,2]. In this model, a virtual photon exchange happens between

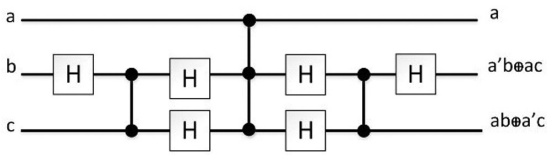

FIG. 3. Quantum circuit realizing a Fredkin gate.

the qubit and the coupled resonator. Therefore, a resonator-mediated coupling can be formed between two qubits coupled to a single resonator. Here, we consider a physical model based on frequency-tunable transmons which are coupled to each other through resonators in a NN architecture. Considering the coupling resonators are not populated, and in the dispersive regime, a first-order perturbative analysis of the Jaynes-Cumming Hamiltonian [7] results in the following effective Hamiltonian [44]:

$$\mathcal{H} = \sum_{k=1}^{n-1} \tilde{\mathcal{H}}_c^{(k,k+1)} + \sum_{k=1}^{n} \tilde{\mathcal{H}}_t^{(k)}. \tag{3}$$

Here, the Hamiltonian of each transmon k is

$$\tilde{\mathcal{H}}_t^{(k)} \equiv \sum_j \tilde{\omega}_j^{(k)} |j\rangle_{(k)}\langle j|, \tag{4}$$

where $\tilde{\omega}_{(j)}^{(k)}$ is the dressed transition frequency associated with the kth transmon at energy level j and is given by

$$\tilde{\omega}_j^{(k)} \equiv j\omega_q^{(k)} + \frac{\delta_k}{2}(j-1)j + \frac{j{g_k}^2}{\omega_q^{(k)} - \omega_r + (j-1)\delta_k}, \tag{5}$$

where $\omega_q^{(k)}$ is the bare transition frequency associated with qubit k; g_k is the coupling strength between transmon k and the connected resonator; and ω_r represents the frequency of the coupled resonator. The last term in Eq. (5) is repeated for each transmon with appropriate modifications depending on the number of coupled resonators.

For any pair of resonator-coupled transmons, we estimate the direct coupling between two transmons $(k,\ k+1)$ as

$$\begin{aligned}\tilde{\mathcal{H}}_c^{(k,k+1)} = \sum_{j_k,\ j_{k+1}} & \sqrt{j_k+1}\sqrt{j_{k+1}+1} J_{j_k,j_{k+1}} \\ & \times (|j_k, j_{k+1}+1\rangle\langle j_k+1, j_{k+1}| \\ & + |j_k+1, j_{k+1}\rangle\langle j_k, j_{k+1}+1|),\end{aligned} \tag{6}$$

where $J_{j_k,j_{k+1}}$ is the estimated direct coupling between the level j_k from the kth transmon and level j_{k+1} from the $(k+1)$th transmon.

$$J_{j_k,\ j_{k+1}} = \frac{g_k g_{k+1}\left(\omega_q^{(k)} + \delta_k j_k - \omega_r + \omega_q^{(k+1)} + \delta_{k+1} j_{k+1} - \omega_r\right)}{2\left(\omega_q^{(k)} + \delta_k j_k - \omega_r\right)\left(\omega_q^{(k+1)} + \delta_{k+1} j_{k+1} - \omega_r\right)}, \tag{7}$$

where δ_k and δ_{k+1} are the anharmonicity values associated with transmons k and $k+1$, respectively.

Note that in order to obtain the effective Hamiltonian using the Schrieffer-Wolff method, the rotating-wave approximation, dispersive approximation, and estimated J coupling were imposed [44]. Other nonlinearities such as cavity anharmonicity due to the Kerr nonlinearity [45] and higher-order transmon level nonlinearities were ignored. Better modeling and

inclusion of higher-order effects will enable higher fidelities of quantum operations on physical systems.

Using the time-dependent Hamiltonian, the time evolution equation of the system is solved to obtain the unitary transformation U:

$$U(t) = \exp\left\{-\frac{i}{\hbar}\int_0^t \mathcal{H}(\tau)\, d\tau\right\}. \tag{8}$$

Here t is time, $\mathcal{H}$ is the Hamiltonian of the system, and $\hbar$ is the reduced Planck's constant. To solve Eq. (8), we employ Trotterization [46]. Hence, the final unitary transformation is estimated as follows [47]:

$$U(t_k) = U_k U_{k-1} U_{k-2} \ldots\ U_2 U_1 U_0. \tag{9}$$

Here U_i for $i = \{0,\ 1,\ \ldots,\ k\}$ is calculated using Eq. (8) for the time-independent Hamiltonian at each time step i, where $U_0 = I$ and k is the total number of steps. The Trotter step size is T/k, where T is the gate evolution time. In our simulations, the Trotter step size was 100 ps.

When solving the time evolution equation, we considered a smaller subspace to reduce the computational expenses. The Hamiltonian for n transmons with four energy levels spans a 4^n-dimensional Hilbert space. For a system composed of three transmons ($n = 3$), the Hamiltonian is a 64×64 matrix operator. Solving the Schrödinger equation for this large operator is computationally expensive, and there are numerous energy levels that have a minimal impact on the evolution of the gate of interest. Thus, we project this larger Hamiltonian to a smaller subspace where at most three excitations are allowed, resulting in a 20×20 matrix [17]. The 20 states considered are $\{|000\rangle, |001\rangle, |002\rangle, |003\rangle, |010\rangle, |011\rangle, |012\rangle, |020\rangle, |021\rangle, |030\rangle, |100\rangle, |101\rangle, |102\rangle, |110\rangle, |111\rangle, |120\rangle, |200\rangle, |201\rangle, |210\rangle, |300\rangle\}$.

The reduced Hamiltonian is evolved based on the qubit transition frequencies. The resulting unitary is projected [17] to the 8×8 computational subspace that includes the states $\{|000\rangle, |001\rangle, |010\rangle, |011\rangle, |100\rangle, |101\rangle, |110\rangle, |111\rangle\}$. Single-qubit phase compensation [13,16,17] is performed on this resultant unitary using the diagonal compensation matrix

$$M = e^{-i\theta_0}\,\mathrm{diag}(1, e^{-i\theta_1}, e^{-i\theta_2}, e^{-i(\theta_1+\theta_2)}, e^{-i\theta_4}, e^{-i(\theta_1+\theta_4)}, e^{-i(\theta_2+\theta_4)}, e^{-i(\theta_1+\theta_2+\theta_4)}), \tag{10}$$

where θ_0 represents the global phase, and θ_1, θ_2, and θ_4 represent the relative single qubit phases of states $|001\rangle$, $|010\rangle$, and $|100\rangle$, respectively.

The single-qubit phases are canceled out by multiplying matrix M with the projected unitary matrix in the computational subspace:

$$U_{\text{final}} = U_{\text{proj}}\, M. \tag{11}$$

Finally, we calculate the gate fidelity $\mathcal{F}$ considering unitarity and closeness to the target ideal operation [48]:

$$\mathcal{F} = \frac{\mathrm{Tr}(U_{\text{final}}^{\dagger} U_{\text{final}}) + |\mathrm{Tr}(U_{\text{ideal}}^{\dagger} U_{\text{final}})|^2}{d(d+1)}, \tag{12}$$

where $d = 2^3$ is the dimensionality of the computational subspace.

V. THE GATE DESIGN METHODOLOGY BASED ON MACHINE LEARNING

We design the system parameters to realize the CCZ and ParChe gates by combining two learning methods:

(1) Modified SUSSADE algorithm.

(2) Our local search algorithm.

In both learning procedures, the gate fidelity [Eq. (12)] is considered as the fitness function to achieve the optimal control parameters for the given ideal unitary matrix. Here, the control parameters are the frequency detuning of transmons. We consider three transmons (*L, M, R*) where transmons *L* and *M* are coupled with an 8.05-GHz resonator, and transmons *M* and *R* are coupled with an 8.2-GHz resonator. In our simulations, the resonator-transmon couplings are $g = 0.2$ GHz, and the anharmonicity of each transmon is $\delta = -0.3$ GHz.

To reduce the search space during the learning procedure, the reference transition frequencies of the qubits are set closer during the ML algorithms search; $f_L = 5.61$ GHz, $f_M = 6$ GHz, and $f_R = 6.39$ GHz, respectively. The maximum frequency detuning ranges (in GHz) permitted from the reference frequency of each qubit are set to [0, 0.5), (−0.5, 0.5), and (−0.5, 0], for qubits *L, M*, and *R*, respectively. These constraints help further reduce the search space and increase the efficiency of the learning process by removing the trial of detuning values far away from the interaction region.

Note that we further impose the following constraints during learning to ensure that the optimal frequency detuning sequences are experimentally realistic, achievable and that the target gate is robust. We enforce these constraints by:

(1) Limiting the maximum point-to-point variation of the frequency detuning of each qubit to 220 MHz within the sequence to prevent undesired excitations in the quantum system. To take into account the limitations of physical signal instrumentation [41], the initial and the final points of the sequence are limited to a maximum point-to-point variation of 500 MHz from the initial reference transition frequencies of 5, 6, and 7 GHz.

(2) Limiting the minimum difference between transition frequencies of two adjacent qubits to 210 MHz/309 MHz for the CCZ/ParChe gate, primarily to prevent interactions within the single-excitation manifold.

Here, we briefly describe how the SUSSADE algorithm [16,17] was used to generate the qubit transition detuning sequences. First, a population of 200 random frequency detuning sequences (chromosomes) is generated in which each sequence contains 150 frequencies (50 per qubit). For a gate duration of $T = 50$ ns, the detuning sequence of each qubit is discretized to 50 amplitudes. After generating the initial population, we perform SUSSADE by randomly modifying the values of detuning sequences using the differential evolution operations such as mutation, crossover, and selection [17,49]. Note that we enforce the realistic constraints on the initial population as well as during the selection operation where after the mutation and crossover, the modified detuning sequences are adjusted properly to meet the desired constraints. Then the resulted detuning sequences are fed to the system Hamiltonian and after time evolution of the Hamiltonian, the fidelity of the resulting gate is calculated using Eq. (12).

For any modified detuning sequence, if the fidelity value is larger than the initial one, the detuning sequence survives to the next generation. This procedure repeats until we reach our choice of either the fidelity threshold value (99.99%) or the maximum number of iterations (one million cycles). We use the Message Passing Interface (MPI) to distribute the simulation to 200 nodes on a computer cluster [50] such that each node is performing a full cycle of solving the time evolution and fidelity calculation for each member of the population.

SUSSADE was successfully used to obtain the frequency detuning sequences for 50-ns three-qubit gates with a fidelity of 98.8%, but any further progress was slow. Thus, a local search algorithm was implemented to refine the detuning sequences and achieve a gate fidelity of >99.9%. Note that the local search algorithm is efficient once the search space has been reduced by other learning algorithms.

The local search algorithm consists of the following steps:

(1) At the beginning of the learning process, we define the largest (100 MHz) and the smallest (1 kHz) change in frequency detuning allowed per data point. This is referred to as the optimization step size ϵ. We also set the maximum number of iterations (1000), the desired fidelity (99.99%), and all constraints enforced during SUSSADE.

(2) While the constraints are met and the desired fidelity or the maximum number of iterations have not been reached, the following procedure is repeated:

(a) A local search window is moved from the first data point toward the last data point.

At each window, the frequency detuning value is varied recursively up or down by the optimization step size ϵ as long as it keeps improving the gate fidelity.

(b) Once the local search window has covered all data points of the detuning sequence of all qubits, ϵ is reduced for a finer grain optimization ($\epsilon_{\text{new}} = 0.1\epsilon_{\text{old}}$).

(c) If the optimization is already completed for the smallest predefined ϵ during the iteration, the iteration number is increased by 1, ϵ is reset to the largest predefined value, and the steps (a) to (d) are repeated.

The three-qubit gate duration is set to 50 ns for evolution, and the learning algorithms operate on 1-ns step size. The learned frequency detuning sequences are kept constant during each 1-ns step to obtain piecewise-constant pulse forms as shown in Fig. 4. Using the Fidelity formula described in Eq. (12), we achieved fidelity of higher than 99.99% for Toffoli gate. For the ParChe gate, we stopped the local search algorithm after reaching the maximum number of iterations and observing the fidelity not to improve beyond 99.975% for many cycles. Therefore, we concluded that with the chosen set of initial system parameters, we achieved the highest fidelity possible for the ParChe gate. Notably a small change in the initial system parameters such as transmon-resonator coupling strength, transmon anharmonicities, resonator frequencies, etc. would open some room for more optimization. However, we did not try to change the chosen initial system parameters to be persistent with the result of 99.99% fidelity CCZ gate with the same chosen parameters. If we would have hit the maximum number of iterations but we had seen improvement in gate fidelity, we could simply rerun the local search optimization algorithm for a second round.

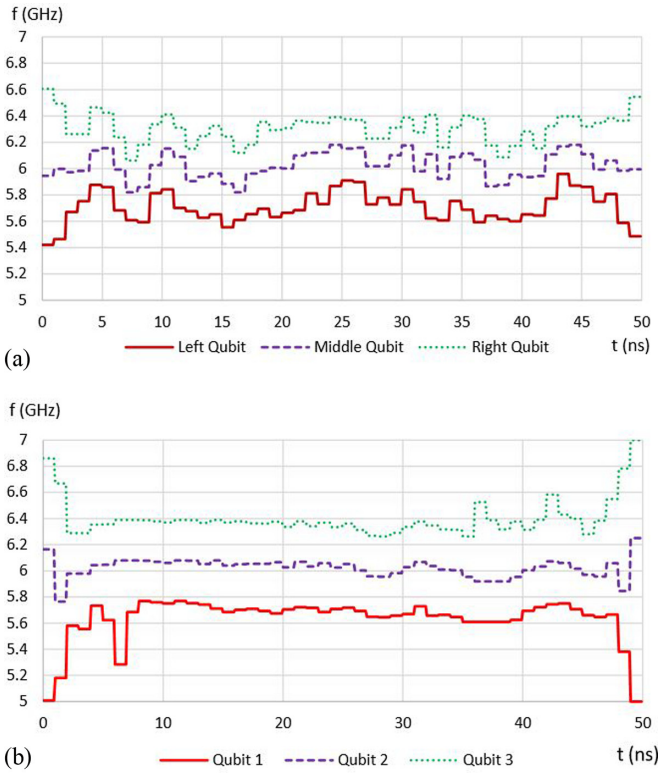

FIG. 4. The frequency (f) vs time (t) plots for learned transition frequency detuning sequences. The piecewise constant forms are generated from the learned frequency detuning sequences (50 learned data points per each transmon). (a) CCZ gate. (b) ParChe gate.

VI. GATE VERIFICATION AND IMPACT OF DECOHERENCE

Simulated quantum process tomography (QPT) was used to independently evaluate gate performances by using master equation simulations. QPT is an excellent tool to evaluate the dynamics of a quantum system due to any process [51], in this case, the CCZ and ParChe gates. Given that this is QPT within the simulation, state preparation and measurement errors do not affect the methodology. Hence the results from QPT enable us to fully characterize the introduced gates.

Initial verification was performed assuming no decoherence in the system by using the von Neumann equation for time evolution:

$$i\hbar\frac{\partial\rho}{\partial t} = \mathcal{H}\rho - \rho\mathcal{H}, \tag{13}$$

where the Hamiltonian $\mathcal{H}$ is the same as that given in Eq. (3) with the number of levels in each transmon set to $j_{\max} = 4$ and ρ is the density matrix for the three-transmon system.

The three-transmon system was evolved using the generated resonance frequency detuning sequences from learning algorithms. The evolution was performed on all the initial states given by $\{I, R_x^{0.5\pi}, R_y^{0.5\pi}, R_x^{\pi}\}^{\otimes 3}|000\rangle$ resulting in 64 density matrices. Unlike experimental QPT, it was not necessary to perform quantum-state tomography to reconstruct these density matrices for the final states. These results were used to perform QPT by imposing constraints that the process matrix χ must satisfy [52,53]. The χ matrix completely

TABLE I. Table of QPT matrices for simulations under different conditions.

Conditions	$\mathcal{F}_p$ CCZ/ParChe	$\mathcal{F}_g$ CCZ/ParChe	$\overline{\mathrm{Tr}(\rho^2)}$ CCZ/ParChe
$k_{\max}=4$ $T_1=T_2=\infty$	0.999/0.999	0.999/0.999	0.999/0.999
$k_{\max}=3$ $T_1=T_2=\infty$	0.998/0.996	0.998/0.997	0.999/0.999
$k_{\max}=4$ $T_1=T_2=20\ \mu$s	0.995/0.994	0.995/0.995	0.991/0.991
$k_{\max}=3$ $T_1=T_2=20\ \mu$s	0.993/0.992	0.994/0.993	0.991/0.991

characterizes the underlying process and is positive Hermitian by definition [51].

We use the following metrics as defined in Ref. [52] to evaluate the performance of the gates:

$$\text{Process fidelity}: \mathcal{F}_{\mathrm{p}} = \mathrm{Tr}(\chi^{(\mathrm{ideal})}\chi), \tag{14}$$

$$\text{Average gate fidelity}: \mathcal{F}_{\mathrm{g}} = \frac{d\mathcal{F}_{\mathrm{p}}+1}{d+1}, \tag{15}$$

$$\text{Average purity}: \overline{\mathrm{Tr}(\rho^2)} = \frac{d\ \mathrm{Tr}(\chi^2)+1}{d+1}, \tag{16}$$

where χ is the experimentally determined process matrix; $\chi^{(\mathrm{ideal})}$ is the ideal process matrix for the gates, and $d=2^3$ is the dimensionality of the computational subspace of the system. The results from the evaluation are given in Table I.

The simulations incorporating decoherence were performed using the Lindblad-Kossakowski form of the master equation [54,55]. The appropriate operators for the dephasing portion of the master equation were obtained as in Refs. [56,57]. For convenience in simulation, T_1 and T_2 were both set to 20 μs, assuming coherence times independent of the flux tuning of the transmons [58]. Please refer to the Appendix for the details of modeling of the qudits in the Lindblad formalism, and full process matrices resulting from QPT. Comparison of results for $k_{\max}=3$ ($\{|0\rangle, |1\rangle, |2\rangle\}$ levels) and $k_{\max}=4$ ($\{|0\rangle, |1\rangle, |2\rangle, |3\rangle\}$ levels) from Table I indicates that the fourth level ($|3\rangle$) also plays a limited role in the system evolution.

VII. ROBUSTNESS EVALUATION

A. Frequency distortion due to smoothing

The frequency detuning sequences derived from the learning algorithms have a piecewise-constant form. To investigate the effect of the first-order distortion due to control electronics, we use the following pulse-reshaping method [13,17] to smooth the frequency detuning sequences:

$$\omega_k(t) = \frac{\omega_{k_i}+\omega_{k_{i+1}}}{2} + \frac{\omega_{k_{i+1}}-\omega_{k_i}}{2}\left[\mathrm{Erf}\left(\frac{t-\left(\frac{t_{\mathrm{ramp}}}{2}\right)}{\sqrt{2}\sigma}\right)\right], \tag{17}$$

where $\omega_k(t)$ represents the distorted frequency detuning of qubit k during $t_i \leqslant t \leqslant t_{i+1}$, and t_i represents the ith time step.

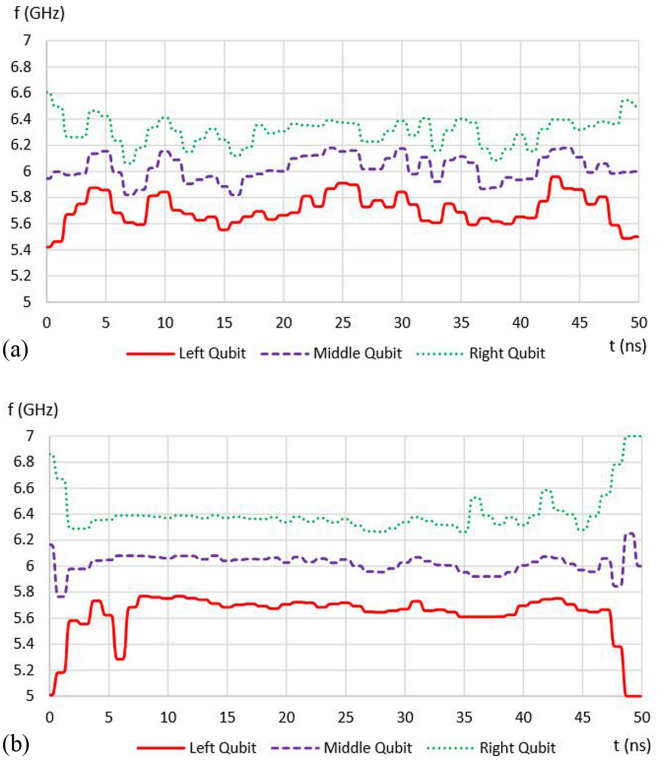

FIG. 5. The frequency (f) vs time (t) plots for the smoothed learned frequency detuning sequences of qubits. (a) CCZ gate. (b) ParChe gate.

Here $\mathrm{Erf}(t) \equiv \frac{2}{\sqrt{\pi}}\int_0^t e^{-x^2}dx$ is the error function value of t, $t_{\mathrm{ramp}}=1$ ns, and $\sigma=\frac{t_{\mathrm{ramp}}}{4\sqrt{2}}$ [13]. The distorted sequences are shown in Fig. 5. Fidelity >99% is observed for both gates with smoothed frequency detuning distortions.

B. Random noise injection

To investigate the effect of random noise on the CCZ and ParChe gates, we plot the average fidelity while increasing the random noise with amplitudes varying from 0 to 10 MHz. For each amplitude value, random noise is generated from a uniform distribution $(-1,\ 1)$, multiplied by the noise amplitude and added to the optimized detuning sequence. The latter step is repeated 10 000 times and at each iteration, the system Hamiltonian is evolved, and the gate fidelity is calculated. The averaged fidelity of the 10 000 results is reported as the average fidelity at each noise amplitude. Figure 6 illustrates the gates' robustness against random noise and demonstrates fidelity >99% with random noise amplitudes of up to 6.7 MHz for CCZ gate and up to 7 MHz for the ParChe gate.

VIII. SHOR'S NINE-QUBIT QEC CIRCUIT BASED ON CCZ AND PARCHE GATES

In order to evaluate the performance of the parity check gate in comparison with the conventional CZ-based parity check, we design the Shor nine-qubit error correction code using ParChe and CCZ gates. Fig. 7 shows a circuit design of Shor's nine-qubit code using Hadamard, ParChe, and CCZ gates.

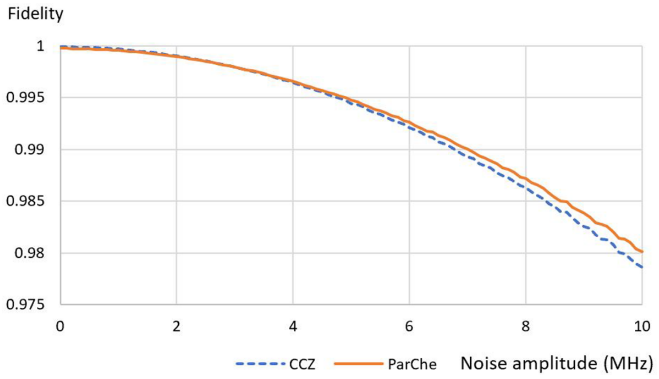

FIG. 6. Average fidelities of CCZ gate and ParChe gate over 10 000 samples under the effect of random noise with amplitudes ranging from 0 to 10 MHz.

The duration of the single-qubit gates, two-qubit CZ gates, and three-qubit (CCZ and ParChe) gates are, respectively, 20 ns, 40 ns [10,23,38–40], and 60 ns (50-ns gate duration+10-ns single-qubit phase compensation). We refer to a state-of-the-art physical model [41] for the duration of single- and two-qubit gates where an extra time is considered for phase compensation through flux control lines. Therefore, we add an extra 10 ns to the duration of our three-qubit gates to accommodate the phase compensation timing.

We use the QX SIMULATOR [59] to simulate the different designs of the Shor's error correction code under noise, where we use the Pauli-Twirling Approximation error model with qubit relaxation time $T_1 = 20\ \mu$s and an echo time $T_2 = 20\ \mu$s. The Pauli-Twirling channel [60,61] allows the approximation of the decoherence channel as an asymmetric depolarizing channel where the decohering qubit suffers from discrete Pauli errors (X, Y, Z) with respective probabilities (p_X, p_Y, p_Z) [62]. The error probabilities are expressed in terms of the gate execution time and the qubit coherence times T_1 and T_2:

$$p_Y = \frac{1}{4}\left[1 - \exp\left(\frac{-t}{T_1}\right)\right] \tag{18}$$

$$p_X = \frac{1}{4}\left[1 - \exp\left(\frac{-t}{T_1}\right)\right] \tag{19}$$

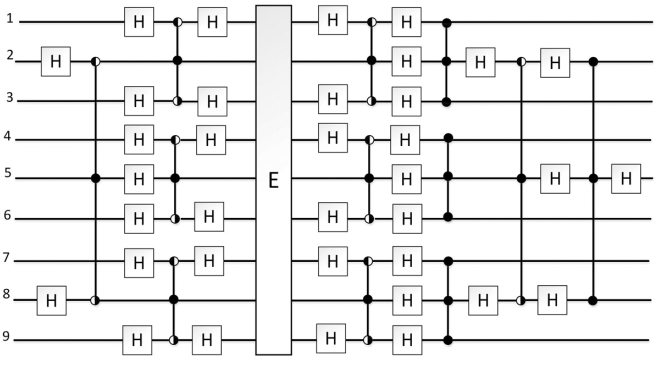

FIG. 7. The proposed Shor's nine-qubit error correction circuit using parity checker gates and CCZ gates. Here, a logical qubit is encoded to nine physical qubits, and E represents an error channel.

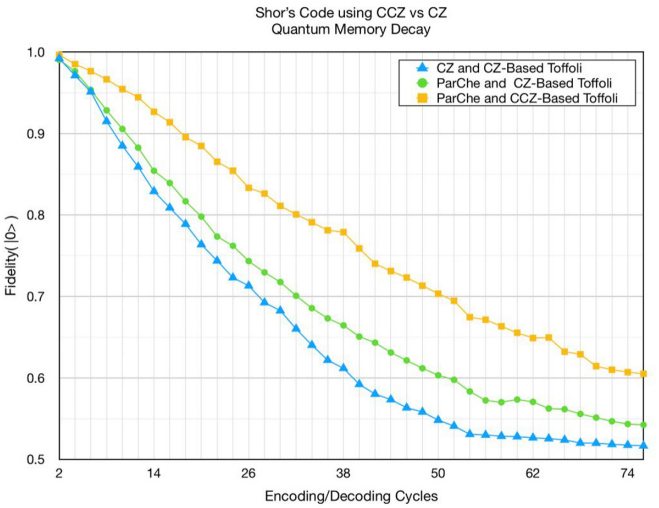

FIG. 8. Performance of a Shor's error correction code under noise when using the ParChe and CCZ gates in comparison with the traditional CZ-based design.

$$p_Z = \frac{1}{2}\left[1 - \exp\left(\frac{-t}{T_2}\right)\right] - \frac{1}{4}\left[1 - \exp\left(\frac{-t}{T_1}\right)\right] \tag{20}$$

For a given density matrix ρ, the approximated amplitude damping (AD) channel is given by

$$\varepsilon_{\mathrm{AD}}(\rho) = E_1^{\mathrm{AD}}\rho E_1^{\mathrm{AD}\dagger} + E_2^{\mathrm{AD}}\rho E_2^{\mathrm{AD}\dagger}. \tag{21}$$

Here E_1^{AD} and E_2^{AD} are the Kraus matrices for the amplitude damping channel:

$$E_1^{\mathrm{AD}} = \begin{pmatrix} 1 & 0 \\ 0 & \sqrt{1-p_{\mathrm{AD}}} \end{pmatrix}, \tag{22}$$

$$E_2^{\mathrm{AD}} = \begin{pmatrix} 0 & \sqrt{p_{\mathrm{AD}}} \\ 0 & 0 \end{pmatrix}, \tag{23}$$

where p_{AD} corresponds to the probability of single-photon emission from the qubit. Similarly, the phase-damping channel can be expressed in terms of Kraus matrices and the action of the two channels combined within a single channel as in Ref. [61].

We compare three designs of the Shor's code:

(1) The CZ-based design where both the parity check stage and the Toffoli gate are implemented in terms of CZ and single-qubit gates.

(2) Replacing only the parity check stage of (1) with the ParChe-based design.

(3) The full three-qubit gate implementation using ParChe-based parity checking and a CCZ-based Toffoli gate.

For each of the Shor's code implementations, we apply many error detection and correction cycles and measure the logical error rate and thus the fidelity. Figure 8 shows the fidelity decay of the logical qubit through the correction cycles of Shor's code. While the fidelity of the logical state decays over the correction cycles due to the low coherence time and the high physical error rate of current systems used in this simulation, the fidelity is significantly improved after introducing the ParChe gate for performing faster parity checks with higher fidelity. The use of the ParChe gate in combination

with the CCZ-based Toffoli provides further improvement and results in a lower logical error rate.

As depicted in Fig. 8, utilizing the ParChe gate reduces the logical error rate as we are mainly limited by the coherence time and the gate duration is an important factor. The CCZ-based Toffoli gate implementation is the major contributor to the improvement in performance, and it relates to both gate count and gate duration.

As both the CZ and three-qubit gates introduced in this work are based on interactions related to avoided-level crossings, the relative improvement in gate times is more relevant as a metric compared to absolute gate time. Given the same coupling strengths between qubits, we expect the relative gate time improvement to remain comparable.

IX. CONCLUSION

We designed two fast, high-fidelity, and robust three-qubit entangling (CCZ and ParChe) gates for resonator-mediated NN-coupled transmons. We described the gate design methodology using simulation and machine-learning techniques and presented a local search algorithm for optimal quantum control applicable to small search spaces. The operations of the CCZ gate and the ParChe gate were confirmed by a C++ simulator that solves the Schrödinger equation for the time-dependent Hamiltonian of the system. Moreover, the operations of the gates were verified independently via quantum process tomography in both the presence and absence of decoherence. The robustness of gates was examined using random noise injection and frequency detuning distortion.

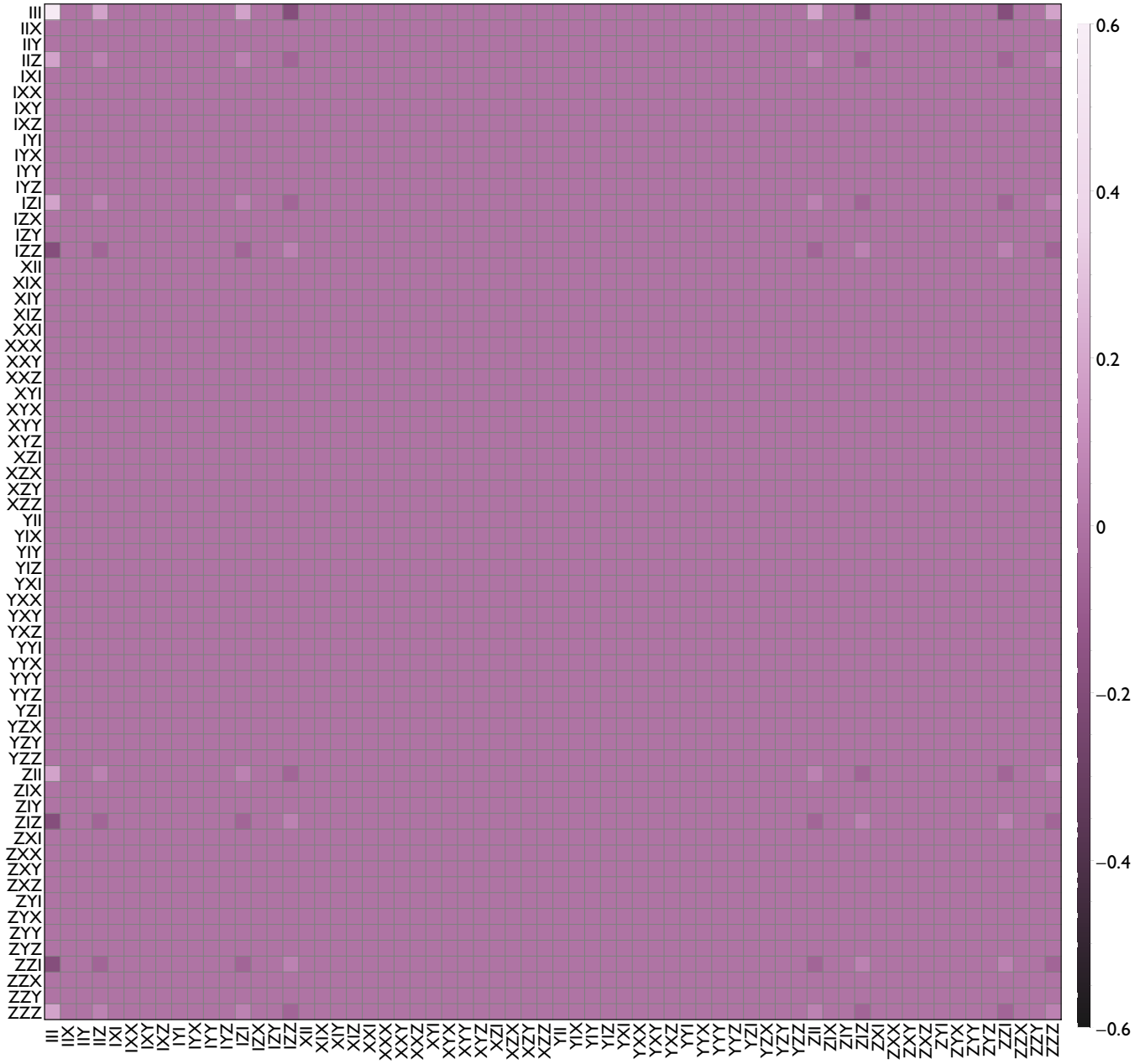

FIG. 9. Real part of the process matrix $\chi^{(\text{ideal})}$ for the ideal CCZ operation. The imaginary component is identically 0 for all elements. The process matrix is expressed in terms of the complete basis set of 64 three-qubit Pauli matrices; I, X, Y, Z represent the matrices σ_0, σ_x, σ_y, σ_z.

The presented gate design procedure, verification, and robustness investigation can be applied to designing gates for other quantum systems as well. We showed that our designed gates can significantly increase the performance of Shor's nine qubit error correction circuit, compared to the traditional circuits based on two-qubit controlled-phase gates. The ParChe gate can be considered as an elementary gate for quantum computing and can be used in quantum arithmetic circuits and many QEC schemes.

ACKNOWLEDGMENTS

This work was made possible in part thanks to Portland Institute for Computational Science and its resources acquired using NSF Grant No. DMS 1624776 and ARO Grant No. W911NF-16-1-0307.

APPENDIX: MODELING DECOHERENCE OF THE TRANSMON SYSTEMS

Lindblad relaxation operators for the transmon qudits were trivially constructed by taking into account the increased photon number for higher levels. The Lindblad dephasing operators were constructed by extending the operator forms presented in Refs. [56,57]. In total, six Lindblad terms were used in the master equation (three terms for relaxation and three terms for dephasing, of each of the transmons). See Figs. 9–12.

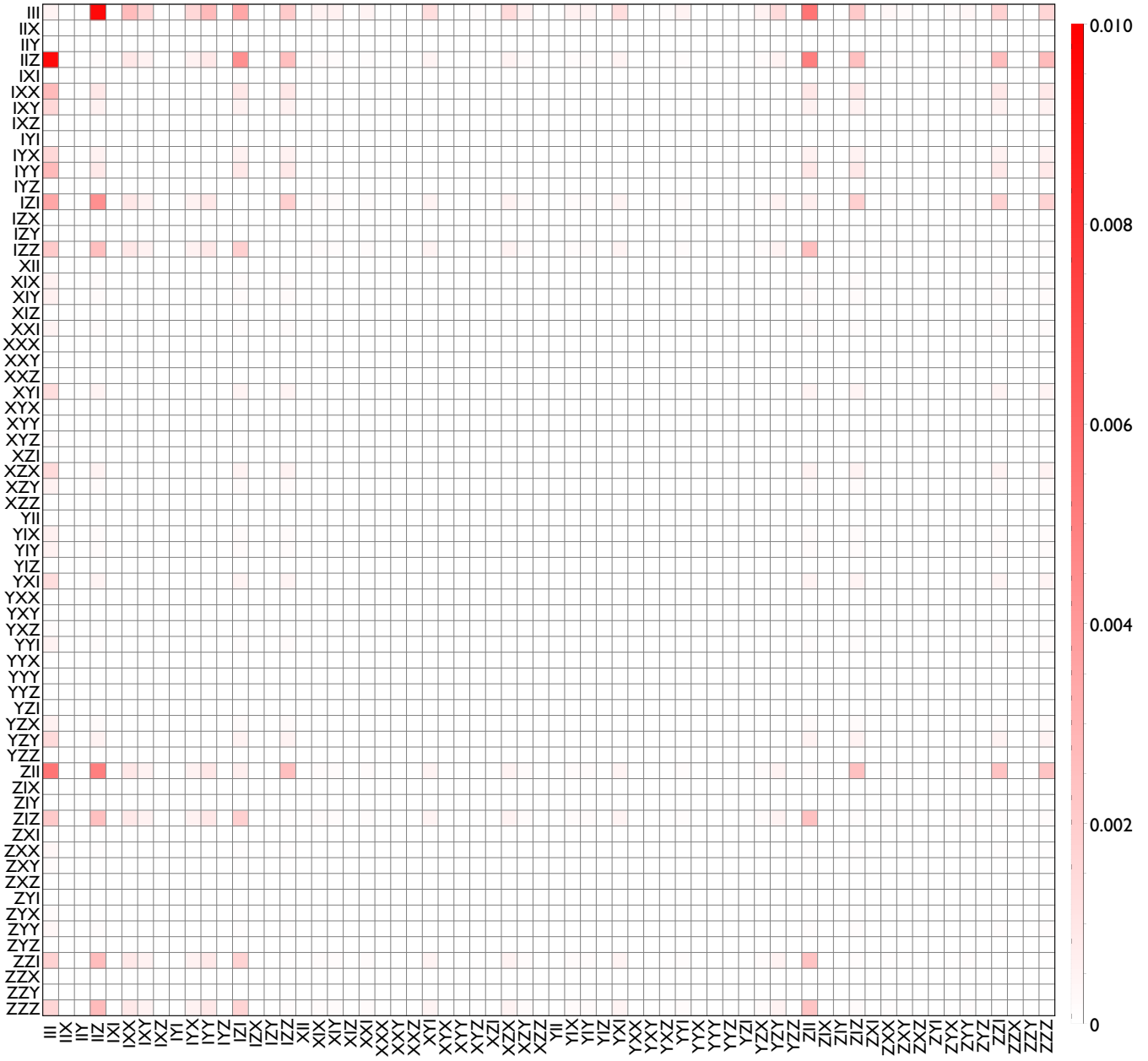

FIG. 10. Absolute values of the differences between elements of ideal and simulated process matrices $[\chi^{(\text{ideal})} - \chi]$ for the ideal CCZ operation. Note the change in legend scale to increase clarity of error terms. The process matrix is expressed in terms of the complete basis set of 64 three-qubit Pauli matrices; I, X, Y, Z represent the matrices σ_0, σ_x, σ_y, σ_z.

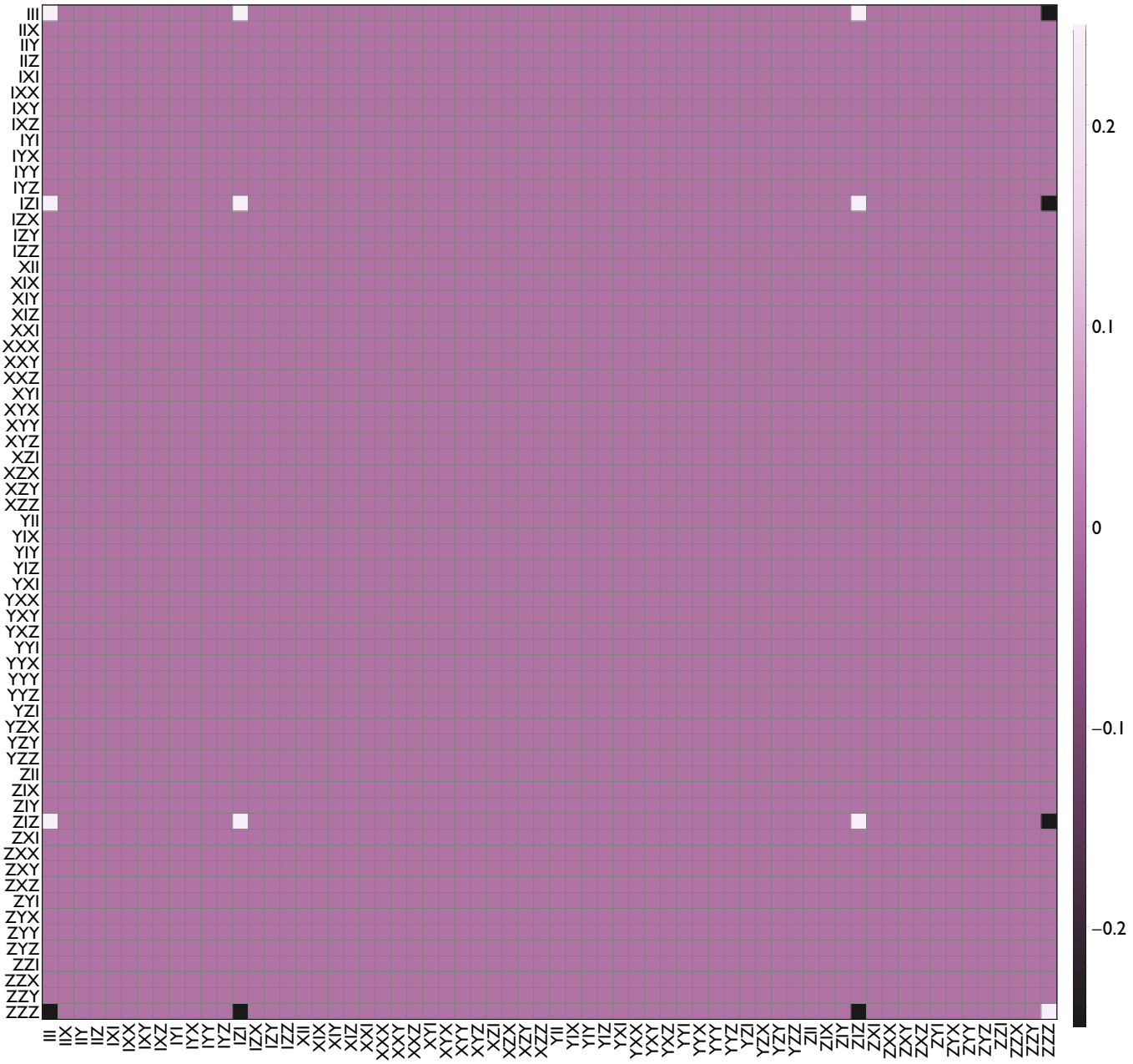

FIG. 11. Real part of the process matrix $\chi^{(\text{ideal})}$ for the ideal ParChe operation. The imaginary component is identically 0 for all elements. The process matrix is expressed in terms of the complete basis set of 64 three-qubit Pauli matrices; I, X, Y, Z represent the matrices σ_0, σ_x, σ_y, σ_z.

For the case of $k_{\max} = 3$, the single-qutrit relaxation and dephasing "jump" operators were

$$A_{\text{rel}} = \begin{pmatrix} 0 & 1 & 0 \\ 0 & 0 & \sqrt{2} \\ 0 & 0 & 0 \end{pmatrix}$$

$$A_{\text{dph}} = \begin{pmatrix} 1 & 0 & 0 \\ 0 & e^{\frac{2\pi i}{3}} & 0 \\ 0 & 0 & e^{\frac{4\pi i}{3}} \end{pmatrix}.$$

For the case of $k_{\max} = 4$, the single-qudit relaxation and dephasing jump operators were

$$A_{\text{rel}} = \begin{pmatrix} 0 & 1 & 0 & 0 \\ 0 & 0 & \sqrt{2} & 0 \\ 0 & 0 & 0 & \sqrt{3} \\ 0 & 0 & 0 & 0 \end{pmatrix}$$

$$A_{\text{dph}} = \begin{pmatrix} 1 & 0 & 0 & 0 \\ 0 & e^{\frac{2\pi i}{4}} & 0 & 0 \\ 0 & 0 & e^{\frac{4\pi i}{4}} & 0 \\ 0 & 0 & 0 & e^{\frac{6\pi i}{4}} \end{pmatrix}.$$

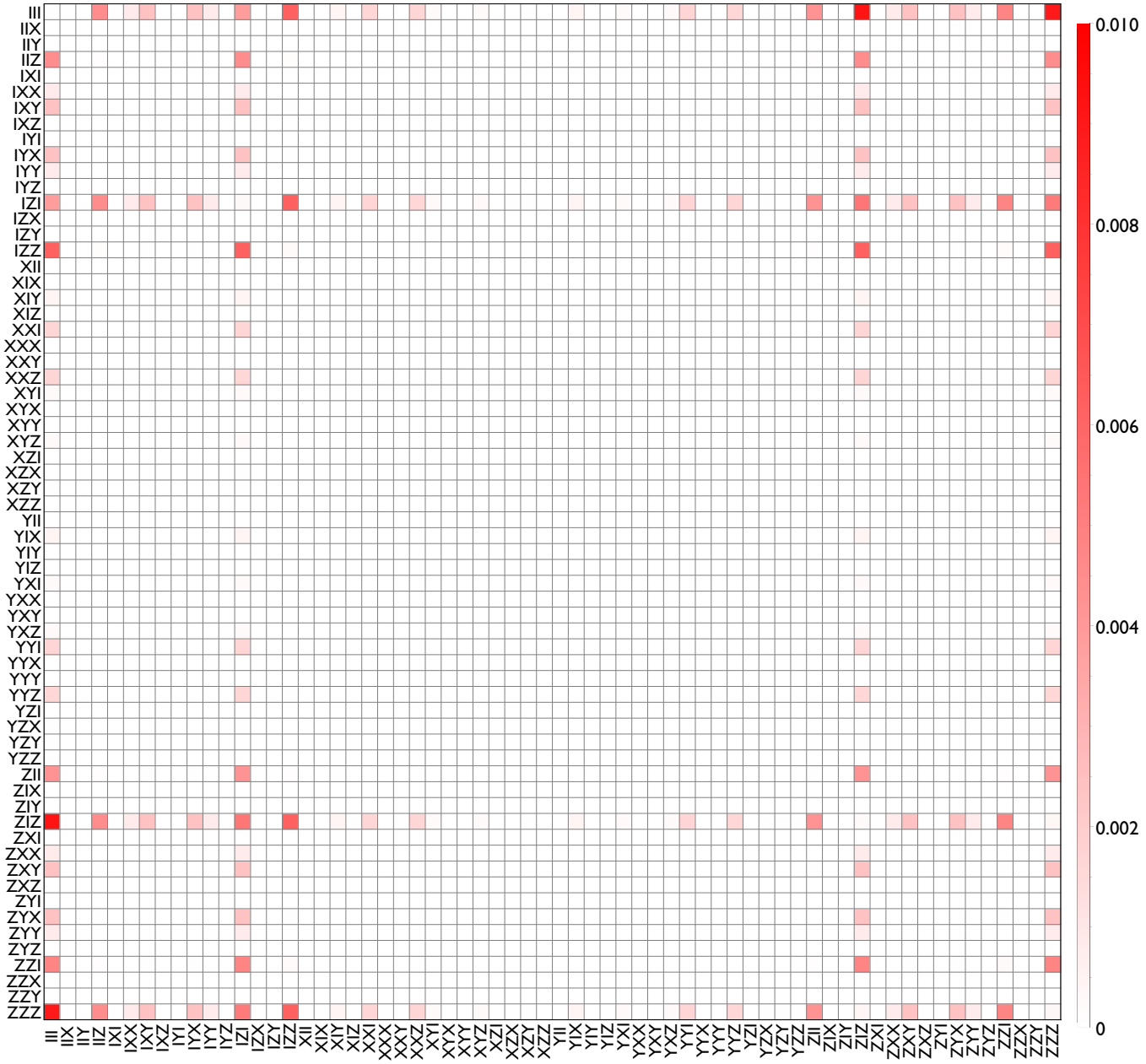

FIG. 12. Absolute values of the differences between elements of ideal and simulated process matrices $[\chi^{(\text{ideal})} - \chi]$ for the ideal ParChe operation. Note the change in legend scale to increase clarity of error terms. The process matrix is expressed in terms of the complete basis set of 64 three-qubit Pauli matrices; I, X, Y, Z represent the matrices σ_0, σ_x, σ_y, σ_z.

Then, the three-qudit relaxation Lindblad terms were constructed using the following operators:

$$A_{\text{rel}} \otimes I \otimes I$$
$$I \otimes A_{\text{rel}} \otimes I$$
$$I \otimes I \otimes A_{\text{rel}}$$

The three-qudit dephasing Lindblad terms were constructed using the following operators:

$$A_{\text{dph}} \otimes I \otimes I$$
$$I \otimes A_{\text{dph}} \otimes I$$
$$I \otimes I \otimes A_{\text{dph}}$$

[1] A. Blais, R. S. Huang, A. Wallraff, S. M. Girvin, and R. J. Schoelkopf, Cavity quantum electrodynamics for superconducting electrical circuits: An architecture for quantum computation, Phys. Rev. A **69**, 062320 (2004).

[2] A. Wallraff, D. I. Schuster, A. Blais, L. Frunzio, R.-S. Huang, J. Majer, S. Kumar, S. M. Girvin, and R. J. Schoelkopf, Strong coupling of a single photon to a superconducting qubit using circuit quantum electrodynamics, Nature (London) **431**, 162 (2004).

[3] J. Koch, T. M. Yu, J. Gambetta, A. A. Houck, D. I. Schuster, J. Majer, A. Blais, M. H. Devoret, S. M. Girvin, and R. J. Schoelkopf, Charge-insensitive qubit design derived from the Cooper pair box, Phys. Rev. A **76**, 042319 (2007).

[4] H. Paik, D. I. Schuster, L. S. Bishop, G. Kirchmair, G. Catelani, A. P. Sears, B. R. Johnson, M. J. Reagor, L. Frunzio, L. I. Glazman, S. M. Girvin, M. H. Devoret, and R. J. Schoelkopf, Observation of High Coherence in Josephson Junction Qubits Measured in a Three-Dimensional Circuit QED Architecture, Phys. Rev. Lett. **107**, 240501 (2011).

[5] R. Barends, J. Kelly, A. Megrant, D. Sank, E. Jeffrey, Y. Chen, Y. Yin, B. Chiaro, J. Mutus, C. Neill, P. O'Malley, P. Roushan, J. Wenner, T. C. White, A. N. Cleland, and John M. Martinis, Coherent Josephson Qubit Suitable for Scalable Quantum Integrated Circuits, Phys. Rev. Lett. **111**, 080502 (2013).

[6] J. M. Gambetta, J. M. Chow, and J. M. Steffen, Building logical qubits in a superconducting quantum computing system, npj Quantum Inf. **3**, 2 (2017).

[7] A. Blais, J. Gambetta, A. Wallraff, D. I. Schuster, S. M. Girvin, M. H. Devoret, and R. J. Schoelkopf, Quantum-information processing with circuit quantum electrodynamics, Phys. Rev. A **75**, 032329 (2007).

[8] J. Preskil, Quantum error correction, Physics 219, Lecture Notes chapter 7, Caltech, http://theory.caltech.edu/people/preskill/ph229/notes/chap7.pdf (accessed 04/29/2020).

[9] B. M. Terhal, Quantum error correction for quantum memories, Rev. Mod. Phys. **87**, 307 (2015).

[10] L. DiCarlo, J. M. Chow, J. M. Gambetta, Lev S. Bishop, B. R. Johnson, D. I. Schuster, J. Majer, A. Blais, L. Frunzio, S. M. Girvin, and R. J. Schoelkopf, Demonstration of two-qubit algorithms with a superconducting quantum processor, Nature (London) **460**, 240 (2009).

[11] F. W. Strauch, Ph. R. Johnson, A. J. Dragt, C. J. Lobb, J. R. Anderson, and F. C. Wellstood, Quantum Logic Gates for Coupled Superconducting Phase Qubits, Phys. Rev. Lett. **91**, 167005 (2003).

[12] R. Barends *et al.*, Superconducting quantum circuits at the surface code threshold for fault tolerance, Nature (London) **508**, 500 (2014).

[13] J. Ghosh, A. Galiautdinov, Z. Zhou, A. N. Korotkov, J. M. Martinis, and M. R. Geller, High-fidelity controlled-σ Z gate for resonator-based superconducting quantum computers, Phys. Rev. A. **87**, 022309 (2013).

[14] A. Fedorov, L. Steffen, M. Baur, M. P. da Silva, and A. Wallraff, Implementation of a Toffoli gate with superconducting circuits, Nature (London) **481**, 170 (2011).

[15] M. D. Reed, L. DiCarlo, S. E. Nigg, L. Sun, L. Frunzio, S. M. Girvin, and R. J. Schoelkopf, Realization of three-qubit quantum error correction with superconducting circuits, Nature (London) **482**, 382 (2012).

[16] E. Zahedinejad, J. Ghosh, and B. C. Sanders, High-Fidelity Single-Shot Toffoli Gate via Quantum Control, Phys. Rev. Lett. **114**, 200502 (2015).

[17] E. Zahedinejad, J. Ghosh, and B. C. Sanders, Designing High-Fidelity Single-Shot Three-Qubit Gates: A Machine-Learning Approach, Phys. Rev. Appl. **6**, 054005 (2016).

[18] M. H. Goerz, F. Motzoi, K. B. Whaley, and C. P. Koch, Charting the circuit QED design landscape using optimal control theory, npj Quantum Inf. **3**, 37 (2017).

[19] S. Machnes, U. Sander, S. J. Glaser, P. de Fouquières, A. Gruslys, S. Schirmer, and T. Schulte-Herbrüggen, Comparing, optimizing, and benchmarking quantum-control algorithms in a unifying programming framework, Phys. Rev. A **84**, 022305 (2011).

[20] R. J. Spiteri, M. Schmidt, J. Ghosh, E. Zahedinejad, and B. C. Sanders, Quantum control for high-fidelity multi-qubit gates, New J. Phys. **20**, 113009 (2018).

[21] N. Khaneja, T. Reiss, C. Kehlet, T. Schulte-Herbrüggen, and S. J. Glaser, Optimal control of coupled spin dynamics: Design of NMR pulse sequences by gradient ascent algorithms, J. Magn. Reson. **172**, 296 (2004).

[22] N. Rach, M. M. Müller, T. Calarco, and S. Montangero, Dressing the chopped-random-basis optimization: A bandwidth-limited access to the trap-free landscape, Phys. Rev. A. **92**, 062343 (2015).

[23] R. Versluis, S. Poletto, N. Khammassi, N. Haider, D. J. Michalak, A. Bruno, K. Bertels, and L. DiCarlo, Scalable Quantum Circuit and Control for a Superconducting Surface Code, Phys. Rev. Appl. **8**, 034021 (2017).

[24] P. W. Shor, Scheme for reducing decoherence in quantum computer memory, Phys. Rev. A **52**, R2493(R) (1995).

[25] A. Peres, Reversible logic and quantum computers, Phys. Rev. A **32**, 3266 (1985).

[26] K. Fazel, M. A. Thornton, and J. E. Rice, ESOP-based Toffoli gate cascade generation, in *2007 IEEE Pacific Rim Conference on Communications, Computers and Signal Processing, Victoria, BC, Canada* (IEEE, 2007).

[27] T. Häner, M. Roetteler, and K. M. Svore, Factoring using 2n+2 qubits with Toffoli based modular multiplication, Quantum Inf. Comput. **17**, 673 (2017).

[28] M. Roetteler, M. Naehrig, K. M. Svore, and K. Lauter, Quantum resource estimates for computing elliptic curve discrete logarithms, in *Advances in Cryptology – ASIACRYPT 2017, Lecture Notes in Computer Science*, edited by T. Takagi and T. Peyrin (Springer, Cham, 2017), Vol. 10625.

[29] Y. Shi, Both Toffoli and controlled-NOT need little help to do universal quantum computing, Quantum Inf. Comput. **3**, 84 (2003).

[30] D. Aharonov, A simple proof that Toffoli and Hadamard are quantum universal, arXiv:quant-ph/0301040.

[31] A. Barenco, C. H. Bennett, R. Cleve, D. P. DiVincenzo, N. Margolus, P. Shor, T. Sleator, J. A. Smolin, and H. Weinfurter, Elementary gates for quantum computation, Phys. Rev. A **52**, 3457 (1995).

[32] V. V. Shende and I. L. Markov, On the CNOT-cost of TOFFOLI gates, Quantum Inf. Comput. **9**, 461 (2009).

[33] E. Alba and M. Tomassini, Parallelism and evolutionary algorithms, IEEE Trans. Evol. Comput. **6**, 443 (2002).

[34] S. B. Kitaev and A. Y. Bravyi, Quantum codes on a lattice with boundary, arXiv:quant-ph/9811052.

[35] E. Dennis, A. Y. Kitaev, A. Landahl, and J. Preskill, Topological quantum memory, J. Math. Phys. **43**, 4452 (2002).

[36] A. G. Fowler, M. Mariantoni, J. M. Martinis, and A. N. Cleland, Surface codes: Towards practical large-scale quantum computation, Phys. Rev. A **86**, 032324 (2012).

[37] G. Yang, W. N. N. Hung, X. Song, and M. Perkowski, Majority-based reversible logic gates, Theor. Comput. Sci. **334**, 259 (2005).

[38] S. A. Cuccaro, T. G. Draper, S. A. Kutin, and D. P. Moulton, A new quantum ripple-carry addition circuit, arXiv:quant-ph/0410184v1.

[39] P. Kumar and S. Daraeizadeh, Parity-based mirror inversion for efficient quantum state transfer and computation in nearest-neighbor arrays, Phys. Rev. A. **91**, 042310 (2015).

[40] C. Albanese, M. Christandl, N. Datta, and A. Ekert, Mirror Inversion of Quantum States in Linear Registers, Phys. Rev. Lett. **93**, 230502 (2004).

[41] M. A. Rol, F. Battistel, F. K. Malinowski, C. C. Bultink, B. M. Tarasinski, R. Vollmer, N. Haider, N. Muthusubramanian, A. Bruno, B. M. Terhal, and L. DiCarlo, Fast, High-Fidelity Conditional-Phase Gate Exploiting Leakage Interference in Weakly Anharmonic Superconducting Qubits, Phys. Rev. Lett. **123**, 120502 (2019).

[42] E. Fredkin and T. Toffoli, Conservative logic, Int. J. Theor. Phys. **21**, 219 (1982).

[43] Y.-B. Sheng and L. Zhou, Distributed secure quantum machine learning, Sci. Bull. **62**, 1025 (2017).

[44] S. Richer, Perturbative analysis of two-qubit gates on transmon qubits, Master's thesis, RWTH Aachen University, 2013.

[45] S. E. Nigg, H. Paik, B. Vlastakis, G. Kirchmair, S. Shankar, L. Frunzio, M. H. Devoret, R. J. Schoelkopf, and S. M. Girvin, Black-Box Superconducting Circuit Quantization, Phys. Rev. Lett. **108**, 240502 (2012).

[46] N. Hatano and M. Suzuki, Finding exponential product formulas of higher orders, in *Quantum Annealing and Other Optimization Methods. Lecture Notes in Physics*, Vol. 679, edited by A. Das and B. K. Chakrabarti (Springer, Berlin, 2005).

[47] M. H. Yung, J. D. Whitfield, S. Boixo, D. G. Tempel, and A. Aspuru-Guzik, Introduction to quantum algorithms for physics and chemistry, *Quantum Physics (quant-ph); Mesoscale and Nanoscale Physics, Advances in Chemical Physics*, Vol. 154, edited by S. Kais (John Wiley & Sons, Hoboken, NJ, 2014).

[48] L. H. Pedersen, K. Molmer, and N. M. Moller, Fidelity of quantum operations, Phys. Lett. A **367**, 47 (2007).

[49] R. Storn and K. Price, Differential evolution–A simple and efficient heuristic for global optimization over continuous spaces, J. Global Optim. **11**, 341 (1997).

[50] Coeus Cluster, http://www.pi4cs.org/equipment.

[51] M. A. Nielsen and I. L. Chuang, *Quantum Computation and Quantum Information* (Cambridge University Press, Cambridge, 2001).

[52] J. L. O'Brien, G. J. Pryde, A. Gilchrist, D. F. V. James, N. K. Langford, T. C. Ralph, and A. G. White, Quantum Process Tomography of a Controlled-NOT Gate, Phys. Rev. Lett. **93**, 080502, (2004).

[53] S. P. Premaratne, J. H. Yeh, F. C. Wellstood, and B. S. Palmer, Implementation of a generalized controlled-NOT gate between fixed-frequency transmons, Phys. Rev. A **99**, 012317 (2019).

[54] G. Lindblad, On the generators of quantum dynamical semigroups, Commun. Math. Phys. **48**, 119 (1976).

[55] A. Kossakowski, On quantum statistical mechanics of non-Hamiltonian systems, Rep. Math. Phys. **3**, 247 (1972).

[56] G. Jaeger and K. Ann, Disentanglement and decoherence in a pair of qutrits under dephasing noise, J. Mod. Opt. **54**, 2327, (2007).

[57] Y. Yang and A. M. Wang, Quantum discord for a qutrit-qutrit system under depolarizing and dephasing noise, Chin. Phys. Lett. **30**, 080302 (2013).

[58] M. D. Hutchings, J. B. Hertzberg, Y. Liu, N. T. Bronn, G. A. Keefe, M. Brink, J. M. Chow, and B. L. T. Plourde, Tunable superconducting qubits with flux-independent coherence, Phys. Rev. Appl. **8**, 044003 (2017).

[59] N. Khammassi, I. Ashraf, X. Fu, C. G. Almudever, and K. Bertels, QX: A high-performance quantum computer simulation platform, in *Design, Automation & Test in Europe Conference & Exhibition (DATE), Lausanne, Switzerland* (IEEE, 2017), pp. 464–469.

[60] M. Silva, E. Magesan, D. W. Kribs, and J. Emerson, Scalable protocol for identification of correctable codes, Phys. Rev. A **78**, 012347 (2008).

[61] J. Ghosh, A. G. Fowler, and M. R. Geller, Surface code with decoherence: An analysis of three superconducting architectures, Phys. Rev. A **86**, 062318 (2012).

[62] P. K. Sarvepalli, A. Klappenecker, and M. Rötteler, Asymmetric quantum codes: Constructions, bounds and performance, Proc. R. Soc. A **465**, 1645 (2009).